Published by IOP Publishing for Sissa Medialab

Received: *April 26, 2023*
Accepted: *May 30, 2023*
Published: *June 22, 2023*

A numerical solver for investigating the space charge effect on the electric field in liquid argon time projection chambers

Shuang Z. Tu,[a,*] **Chao Jiang,**[a] **Thomas R. Junk**[b] **and Tingjun Yang**[b]

[a]*Department of Electrical and Computer Engineering and Computer Science, Jackson State University, Jackson, MS 39217, U.S.A.*
[b]*Neutrino Division, Fermi National Accelerator Laboratory, Batvia, IL 60510, U.S.A.*

E-mail: shuang.z.tu@jsums.edu

Abstract: This paper reports the development of a numerical solver aimed to simulate the interaction between the space charge (i.e. ions) distribution and the electric field in liquid argon time projection chamber (LArTPC) detectors. The ion transport equation is solved by a time-accurate, cell-centered finite volume method and the electric potential equation by a continuous finite element method. The electric potential equation updates the electric field which provides the drift velocity to the ion transport equation. The ion transport equation updates the space charge density distribution which appears as the source term in the electric potential equation. The interaction between the space charge distribution and the electric field is numerically simulated within each physical time step. The convective velocity in the ion transport equation can include the background flow velocity in addition to the electric drift velocity. The numerical solver has been parallelized using the Message Passing Interface (MPI) library. Numerical tests show and verify the capability and accuracy of the current numerical solver. It is planned that the developed numerical solver, together with a Computational Fluid Dynamics (CFD) package which provides the flow velocity field, can be used to investigate the space charge effect on the electric field in large-scale particle detectors.

Keywords: Detector modelling and simulations II (electric fields, charge transport, multiplication and induction, pulse formation, electron emission, etc); Simulation methods and programs

*Corresponding author.

https://doi.org/10.1088/1748-0221/18/06/P06022

2023 JINST 18 P06022

Contents

2023 JINST 18 P06022

1 Introduction

The Deep Underground Neutrino Experiment (DUNE) [1] will employ several particle detectors in a beam of neutrinos produced at Fermi National Accelerator Laboratory in Batavia, IL. The near detectors will be located on the Fermilab site, and the far detectors will be located at the Sanford Underground Research Facility in Lead, SD. One of the three primary purposes of the experiment is to measure the properties of neutrinos as they travel 1300 km through the earth. They are expected to oscillate from one flavor of neutrino to another and back as they travel. Measuring the flavor transition probabilities will tell us about the masses, mixings, and charge-parity (CP) symmetry violating properties of neutrinos. CP violation is a necessary ingredient to explain why there is more matter in the universe than there is antimatter. The second primary purpose is to detect neutrinos from supernova bursts within the Milky Way galaxy and nearby dwarf galaxies such as the Magellanic Clouds. The third purpose is to search for nucleon decay, which is predicted by some grand unified theories. Before building the large far detector modules, each of which will contain 10 kt of fiducial mass of liquid argon, prototypes have been built and additional prototypes will

be built in order to test the design and the robustness of the components. Two large prototypes, ProtoDUNE-SP [2] and ProtoDUNE-DP [3, 4] are located at CERN in a test beam.

1.1 Liquid argon time projection chamber

The primary particle detection technology chosen for the large far detector modules is the liquid argon time projection chamber (LArTPC). A LArTPC contains a volume of highly purified liquid argon (LAr) in a strong electric field, provided by a planar cathode and a planar anode. High-speed charged particles such as cosmic rays or particles produced in neutrino interactions will ionize argon atoms along the particle trajectories. Some of the electrons that are freed in the ionization drift in the electric field, scattering from the argon atoms but they are not absorbed. Other electrons freed by ionization recombine with the positive argon ions, producing flashes of scintillation light. If the argon is sufficiently free of electronegative impurities such as oxygen and water, then the drifting electrons will travel to the anode.

This paper focuses on the ProtoDUNE-SP geometry. In this detector, two anode planes are on the outside faces of the detector, facing the cryostat, and one vertically hung cathode plane is in the middle, while the far detector contains additional planes [5]. The distance between the cathode plane and the nearest anode plane is 3.6 m in both the far detector and in ProtoDUNE-SP. The nominal electric field strength is 500 V/cm. The potential on the cathode is −180 kV, and the anode plane contains elements at ground potential. A field cage consisting of an array of metal profiles that are held at electrical potentials that linearly vary with their position between the cathode and the anode shape the field, providing as close to a uniform field as possible within the volume of liquid argon (cf. figure 1). Ten photon detectors are located between the grounded mesh planes inside each APA frame.

The anode plane is made up of charge-sensing elements. In a single-phase LArTPC, it consists of four planes of wires — a grid plane, two induction planes (U and V), and a collection plane (X). A grounded mesh lies behind the collection plane. The potentials are set on the wire planes so that charge drifts past the grid wires and the wires in the two induction planes but collects on the collection plane. Sensitive amplifiers and digitizers are attached to each induction-plane wire and each collection-plane wire. The wires are attached to frames called Anode Plane Assemblies (APAs). Wire anode planes are strung on both sides of the APA. The collection-plane wires run the lengths of the APA, while the induction-plane wires are arranged at ±35.7° from the vertical collection-plane wires. Induction-plane wires are wrapped around the sides of the APA frames, held in place with FR-4 wire boards. The grid wires are not instrumented for readout, but they provide signal shaping and electrostatic protection.

The general operating principle of the single phase LArTPC is as follows. Negatively charged ionization electrons produced in interactions between energetic charged particles and the argon in the detector drift horizontally through the LAr in the direction opposite to the electric field and are collected on the anode. Photon detectors will provide the t_0 of the interaction. The drifting charges induce bipolar signals on the U and V wires and unipolar signals on the X wires (cf. figure 2). The arrival time of the drifting charge, together with knowledge of the drift velocity of the electrons in the applied field, allows the determination of the distance from the ionization point to the anode, provided that the time of the original ionization is known. This time can be known either from the timing of the beam pulse from Fermilab, or, in the case of natural sources such as comic rays, the time of the scintillation light flashes.

2023 JINST 18 P06022

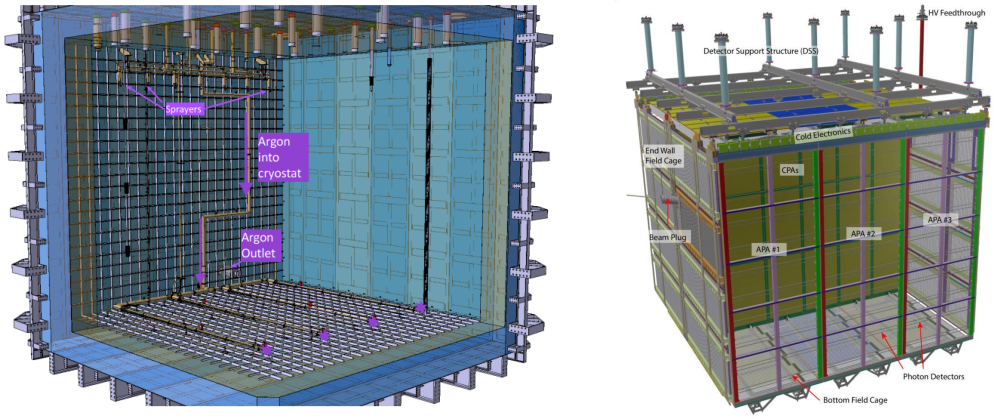

Figure 1. Sketch of the cryostat interior (left) and the field cage (right) of the ProtoDUNE-SP detector. Reproduced from [5]. © 2020 CERN. CC BY 4.0.

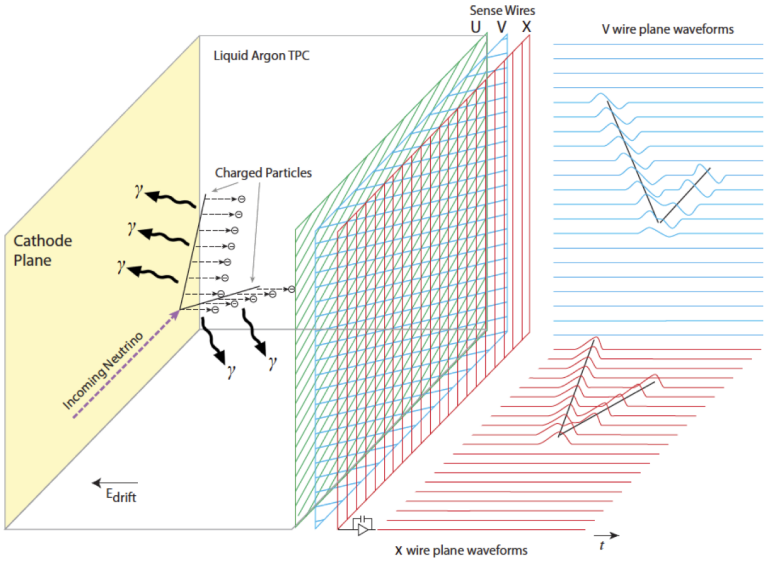

Figure 2. The general operating principle of the single phase LArTPC. Negatively charged ionization electrons from the neutrino interaction drift horizontally opposite to the E field in the LAr and are collected on the anode, which is made up of the U, V and X sense wires. The right-hand side represents the time projections in two dimensions as the event occurs. Photon detectors (not shown) will provide the t_0 of the interaction. Reproduced from [1]. © 2020 CERN. CC BY 4.0.

2023 JINST 18 P06022

1.2 The effect of space charge

For LArTPCs located the Earth's surface, such as ProtoDUNE-SP, cosmic rays constantly impinge on the detector. While the drifting electrons are quickly swept away by the applied electric field, the remaining positively charged argon ions drift very slowly, on the order of several centimeters per second. This speed is comparable to the fluid flow speed. Positive ions therefore may accumulate somewhere in the active volume of the LArTPC, and cause distortions of the electric potential from its nominal form [6]. Negatively-charged ions created when electrons attach to impurities (oxygen or water molecules) also are expected to drift slowly, though their concentrations are small if the LAr is very pure. The resulting distortions in the electric field cause drifting electrons to arrive at different places and at different times on the anode plane than they would had there been no distortions. The distorted electric field also changes the fraction of electrons that recombine with the argon ions. Measurements of the positions of track endpoints can help constrain space-charge distortion effects [7, 8].

The liquid argon flow velocity distribution can be obtained by solving incompressible Navier-Stokes equations using a Computational Fluid Dynamics solver. For example, various commercial Computational Fluid Dynamics (CFD) packages including ANSYS CFX and Star-CCM+ have been used to calculate the flow motion [9–11]. However, this paper focuses on the development of a separate numerical solver for simulating the interaction between the space charge distribution and the electric field. The flow velocity field is one of the inputs to the current solver.

1.3 Mathematical modeling

The transport of ions can be modeled as

$$\frac{\partial \rho_c}{\partial t} + \nabla \cdot [(\mathbf{u} + \mathbf{u}_d)\rho_c] = \nabla \cdot (D\nabla\rho_c) + S \tag{1.1}$$

where ρ_c is the charge density of the positive ion. In this paper, we consider positive ions only as this paper aims to demonstrate the capability in simulating the interaction between the ion distribution and the electric field. Negative ions due to electron attachment to impurities will be considered in our future work.

$\mathbf{u}$ in eq. (1.1) is the background flow velocity vector, D is the diffusion coefficient, V is the electrostatic potential and S is the source/sink term (for example, charge injection due to cosmic rays, electron-ion production in high-energy interactions, electron-ion recombination, electron-impurity attachment and ion-ion neutralization). Electrons drift with a velocity of roughly 1.6 mm/µs and thus do not contribute significantly to the accumulated space charge. The drift velocity of the ions, $\mathbf{u}_d$, due to the electric field is obtained via

$$\mathbf{u_d} = \mu\mathbf{E} \tag{1.2}$$

with μ being the mobility of the ions and $\mathbf{E}$ the electric field. Note that there is an uncertainty in the value of the mobility of the ions. The measured value of the mobility depends on experimental conditions such as the impurity level and temperature. In this paper we choose the value adopted in ref. [12], namely, $\mu = 1.6 \times 10^{-7}\mathrm{m}^2\mathrm{V}^{-1}\mathrm{s}^{-1}$.

The diffusion coefficient D in eq. (1.1) can be determined from the Einstein relation

$$D = \frac{\mu k_\mathrm{B} T}{q} \tag{1.3}$$

2023 JINST 18 P06022

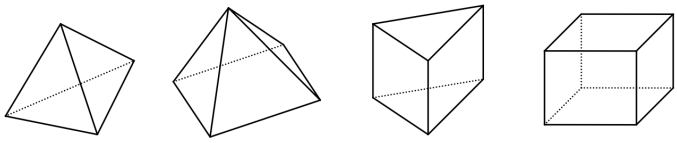

Figure 3. 3D element types that can be handled by the current solver: tetrahedron, pyramid, prism and hexahedron.

where k_B is the Boltzmann constant (= $1.380649 \times 10^{-23} \mathrm{J \cdot K^{-1}}$), q is the electric charge of a positive ion (= 1.602×10^{-19}C) and T is the temperature in Kelvin (K).

The electric field $\mathbf{E}$ is related to the electric potential V via

$$\mathbf{E} = -\nabla V. \tag{1.4}$$

The electrostatic potential V satisfies the following Poisson equation according to Gauss's law

$$-\nabla \cdot (\nabla V) = \frac{\rho_c}{\varepsilon} \tag{1.5}$$

where ε is the permittivity of the medium which is defined as follows:

$$\varepsilon = \varepsilon_r \varepsilon_0, \tag{1.6}$$

with ε_r the relative permittivity (i.e., the dielectric constant, $\varepsilon_r = 1.504$ for liquid argon) for the medium and $\varepsilon_0 = 8.854 \times 10^{-12}$ F/m the permittivity of free space (a vacuum).

In this paper, we describe a numerical package we have developed to solve the space charge transport equation (1.1) coupled with the electrostatic potential equation (1.5) in an arbitrary spatial domain. The resulting package can be used to investigate the space charge effect on the electric field in the LArTPC detectors.

This paper is organized as follows. Section 2 briefly describes the numerical methodology used to solve eqs. (1.1) and (1.5). In section 3, several numerical test cases are presented to demonstrate i) the space charge effect on the electric field and ii) the accuracy of current numerical methods by comparing the numerical results with analytical solutions. Finally section 4 provides the summary of this work and discussions about future work.

2 Numerical methodology

The present numerical methodology is adapted from our in-house incompressible flow solver [13, 14] where a hybrid finite volume/element method is used. The resulting numerical solver is able to solve both 2-D and 3-D problems with the computational domain discretized by hybrid elements (cf. figure 3). In addition, since the solver is parallelized using the Message Passing Interface (MPI) library, the solver is able to solve large-scale problems on parallel computing systems. This section briefly describes the methodology in developing the current numerical solver.

2023 JINST 18 P06022

2.1 Nondimensionalization of equations

The actual values of the physical quantities in eqs. (1.1) and (1.5) vary a lot in magnitude in SI units. It is desirable to use an appropriate set of reference values to nondimensionalize and scale the dimensional values such that all dimensionless values are within a magnitude range close to 1. Independent primary reference values are as follows:

- ρ_{ref}: reference charge density.
- L_{ref}: reference length.
- u_{ref}: reference velocity.
- V_{ref}: reference electric potential.

Other derived reference values include

- $t_{\text{ref}} = L_{\text{ref}}/u_{\text{ref}}$: reference time scale,
- $E_{\text{ref}} = V_{\text{ref}}/L_{\text{ref}}$: reference electric field,
- $\mu_{\text{ref}} = u_{\text{ref}}/E_{\text{ref}}$: reference positive ion mobility,
- $D_{\text{ref}} = L_{\text{ref}}u_{\text{ref}}$: reference diffusivity,
- $S_{\text{ref}} = \rho_{\text{ref}}u_{\text{ref}}/L_{\text{ref}}$: reference source term and
- $\varepsilon_{\text{ref}} = \rho_{\text{ref}}L_{\text{ref}}^2/V_{\text{ref}}$: reference permittivity.

It can be easily shown that the resulting dimensionless equations are mathematically identical to the original ones.

2.2 Finite volume method for the space charge transport equation

The space charge transport equation (1.1) is a linear advection-diffusion equation. Here an implicit cell-centered finite volume method (FVM) is used to discretize this equation. The backward Euler difference formula (BDF) is adopted for the time integration. For each cell i, the finite volume discretization leads to

$$\frac{c_1\rho_c^{n+1} + c_0\rho_c^n + c_{-1}\rho_{\mathbf{c}}{}^{n-1}}{\triangle t} + R\left(\rho_c^{n+1}\right) = 0 \quad \text{for each cell} \tag{2.1}$$

where ρ_c is the cell average of the unknown at cell i. Here the spatial subscript i is omitted for notational simplicity. The superscript n denotes the time level. Therefore, ρ_c^{n+1} represents the solution at the new time level $n+1$. Δt is the time step. R contains the advective, diffusive and the source terms as follows:

$$R = \frac{1}{\left|\Omega_i\right|}\int_{\partial\Omega_i} \mathbf{H}\cdot\mathbf{n}\mathrm{d}\Gamma + \frac{1}{\left|\Omega_i\right|}\int_{\Omega_i} S\mathrm{d}\Omega.$$

Here $\mathbf{H}$ includes both advective and diffusive fluxes, $\mathbf{n}$ is the outward unit normal of the faces $\partial\Omega_i$ surrounding cell i and $|\Omega_i|$ is the volume of cell i. The detailed implementation of the second-order accurate advective and diffusive fluxes can be found in ref. [13] and is not repeated here.

2023 JINST 18 P06022

The coefficients c_1, c_0 and c_{-1} in eq. (2.1) depend on whether first order (BDF1) or second order (BDF2) time integration is used. For BDF1, $c_1 = 1.0$, $c_0 = -1.0$ and $c_{-1} = 0.0$. For BDF2, $c_1 = 1.5$, $c_0 = -2.0$ and $c_{-1} = 0.5$.

The system of eq. (2.1) for all cells can be written in vector form as

$$\mathbf{G}(\boldsymbol{\rho}_c^{n+1}) = 0 \tag{2.2}$$

where the bold symbol $\boldsymbol{\rho}_c$ contains all unknowns at each of the cells. Instead of solving eq. (2.2) directly, the following system is solved for the solution increment $\delta\boldsymbol{\rho}_c$

$$\mathbf{J}\delta\boldsymbol{\rho}_c = -\mathbf{G}(\boldsymbol{\rho}_c^{n+1}) \tag{2.3}$$

where $\mathbf{J}$ is the Jacobian matrix and can be computed as

$$\mathbf{J} \equiv \frac{\partial \mathbf{G}}{\partial \boldsymbol{\rho}_\mathbf{c}} = \frac{c_1}{\triangle t}\mathbf{I} + \frac{\partial \mathbf{R}}{\partial \boldsymbol{\rho}_c} = \frac{c_1}{\triangle t}\mathbf{I} + \tilde{\mathbf{J}} \tag{2.4}$$

where $\tilde{\mathbf{J}}$ represents the contribution to $\mathbf{J}$ from the spatial flux terms and the source term $\mathbf{R}$, and $\mathbf{I}$ is the identity matrix.

For large-scale problems with discretization based on compact schemes, the resulting linear system is usually huge, sparse and ill-conditioned. The Generalized Minimal RESidual method (GMRES) [15] has been widely used to solve this kind of linear systems. As a Krylov subspace method, the GMRES algorithm involves only matrix-vector multiplication. Therefore, it is unnecessary to form the Jacobian matrix explicitly. The matrix-vector product can be approximated using a matrix-free technique [13, 16]. The convergence performance of the GMRES algorithm is highly related to the preconditioning. The Lower-Upper Symmetric Gauss Seidel (LU-SGS) preconditioning explained in [13, 16] is employed to significantly improve the convergence performance.

2.3 Finite element method for the electrostatics Poisson equation

The nodal Galerkin finite element method (FEM) is chosen to discretize the electrostatics Poisson equation. The unknown V_i is placed at each of the mesh vertices. With the help of nodal basis functions, one can express V at any location in the computational domain using the solutions at vertices

$$V = \sum_{j=1}^{\mathrm{nv}} \phi_j V_j \tag{2.5}$$

where $\{\phi_j\}_{j=1}^{\mathrm{nv}}$ are the nodal basis functions and nv is the number of vertices of the mesh. The basis function is Lagrangian defined in each element. Therefore, the solution is arbitrarily continuous inside each element and has C^0 continuity on element borders.

The variational form of eq. (1.5) is obtained by multiplying eq. (1.5) with each of the shape functions and integrating over the entire domain Ω by parts as follows

$$\int_\Omega \nabla\phi_i \cdot \nabla V \mathrm{d}\Omega = \int_\Omega \phi_i \frac{\rho_c}{\varepsilon}\mathrm{d}\Omega + \int_\Gamma \phi_i \left(\mathbf{n}\cdot\nabla V\right)\mathrm{d}\Gamma \quad i = 1, \cdots, \mathrm{nv} \tag{2.6}$$

Substituting eq. (2.5) into eq. (2.6) results in a sparse and symmetric linear system. The preconditioned conjugate gradient method is employed to solve this system. The coefficient matrix (stiffness matrix) is explicitly formed using the compressed sparse row format. The preconditioning is based on the Incomplete Lower-Upper (ILU(0)) decomposition.

2023 JINST 18 P06022

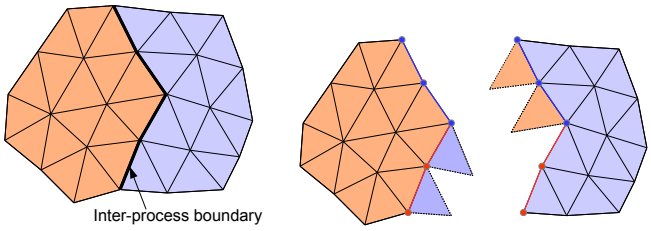

Figure 4. Mesh partitioning.

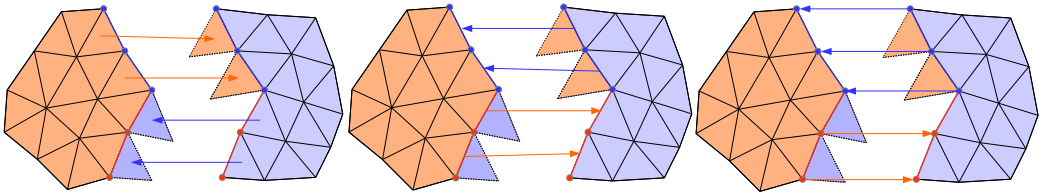

Figure 5. Inter-process communication. Left: element communication. Middle: face communication. Right: vertex communication.

2.4 Parallelization of the numerical solver

To solve large scale problems, the current numerical solver is parallelized using the Message Passing Interface (MPI) library to access multiple processors simultaneously and speed up computation. The choice of the MPI parallel paradigm is due to its standardization, excellent platform-independent portability and flexibility on both distributed-memory and shared-memory machines. Parallelism is achieved via the Single Program Multiple Data (SPMD) principle. The computational mesh is first partitioned across certain number of processes using the ParMETIS library [17] (cf. figure 4). The partitioning ensures the number of elements is roughly the same on each of the processes for the purpose of balancing the load. In addition, ParMETIS also minimizes the inter-process communication overhead. The same numerical solver program is then executed on each of the processes on its portion of the mesh simultaneously. Inter-process communication occurs to synchronize the computation. Since the current cell-centered finite volume and nodal finite element solvers are constructed on compact computational stencils, the inter-processor communication involves only nodes, faces and elements on the partition boundaries (cf. figure 5). This compactness makes it trivial to attain high parallelizability using MPI for fixed-topology meshes. Very efficient non-blocking MPI functions can be called to set up the inter-processor "gather" and "scatter" routines in the pre-processing stage [16, 18]. The communication overhead has been minimized thanks to these routines.

3 Numerical tests and discussions

In this section, a simplified 3-D chamber of rectangular shape is used to model the geometry of a LArTPC detector. More specifically, the dimension data (3.6m $\times$ 6m $\times$ 6m) of the ProtoDUNE-SP geometry [2] is used to construct the computation domain $[-3.6, 0] \times [-3, 3] \times [-3, 3]$, namely, $L_x = 3.6\,\text{m}$ and $L_y = L_z = 6\,\text{m}$. The anode plane is located at $x = 0\,\text{m}$ and the cathode plane is at

2023 JINST 18 P06022

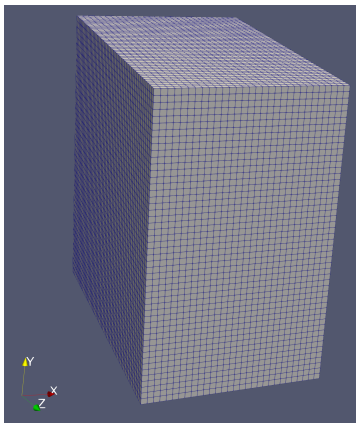

Figure 6. Computational domain and mesh.

$x = 3.6$m. The remaining boundaries are the field cage walls. Even though the current numerical solver is developed to handle unstructured meshes, a structured hexahedral mesh is used to discretize the current simple geometry. The mesh resolution is $30 \times 50 \times 50$ with 75,000 hexahedral elements, as shown in figure 6.

The following input parameters are given for the simulation:

- source term $S = 2 \times 10^{-10}\text{Cm}^{-3}\text{s}^{-1}$,
- nominal electric field: $E_\circ = 500\text{V/cm}$,
- dielectric constant $\varepsilon_r = 1.504$ and permittivity of free space $\varepsilon_0 = 8.854 \times 10^{-12}$ F/m,
- mobility $\mu = 1.6 \times 10^{-7}\text{m}^2\text{V}^{-1}\text{s}^{-1}$, and
- diffusion coefficient $D = 1.2134543 \times 10^{-9}\text{m}^2/\text{s}$.

Based on the above input parameters, the dimensionless parameter defined in eq. (A.7) $\alpha = 0.69758$. The time needed for ions to travel from the anode plane to the cathode plane $T = L_x/(\mu E_\circ) = 450$s. In all current simulations, the time step is chosen as $\Delta t = 7.5$s. Six CPU cores are used in parallel for this relatively small mesh.

The simulation continues until the steady state has been reached. In the plots shown in this section, the space charge density is normalized by $\rho_\circ$ which is defined by $\rho_\circ \equiv \varepsilon E_\circ/L_x = 1.8495 \times 10^{-7}\text{Cm}^{-3}$, and the electric field is normalized by $E_\circ$.

3.1 Simulations without diffusion

We first consider the cases where the diffusive effect in space charge transport is neglected. Equation (1.1) then becomes

$$\frac{\partial \rho_c}{\partial t} + \nabla \cdot [(\mathbf{u} + \mathbf{u}_d)\rho_c] = S \tag{3.1}$$

Results obtained will be compared with the 1-D analytical solutions, if available. In the derivation of 1-D analytical solutions, the diffusion term was omitted.

2023 JINST 18 P06022

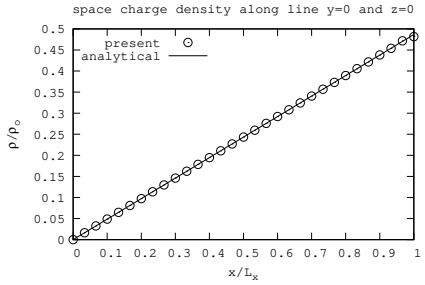

Figure 7. Case I: normalized space charge density distribution along the line defined by $y = 0$ and $z = 0$ in the case of uniform electric field.

3.1.1 Case I: space charge transport under uniform electric field

We first consider a case where the electric field is assumed not distorted by the space charge distribution, i.e. the electric field takes the uniform nominal value in x-direction across the chamber. This is the case considered in Reference [8]. Therefore, only the space charge transport equation (3.1) is solved. The space charge is expected to be linearly distributed along the x-direction. The boundary conditions are set as follows: Dirichlet condition $\rho_c = 0$ at the anode plane and open boundary condition at the cathode plane and at field cage walls. Figure 7 shows the normalized space charge density along the line defined by $y = 0$ and $z = 0$. The analytical solution, which is given in eq. (A.3), is a linear function of x, and it is also shown in figure 7. The numerical solution matches the analytical solution. Please be aware that in all the figures presented within this section, the horizontal axis of the numerical solution has been adjusted to fit within the range of $[0, 1]$.

3.1.2 Case II: interaction between the space charge transport and the electric field

This case couples the space charge transport equation (3.1) and the electric potential Poisson equation (1.5) in each time step in the simulation. Since the space charge density appears in the source term of the potential Poisson equation and the electrical potential can be used to derive the electric field which in return appears in the calculation of the drift velocity in the space charge transport equation, the coupled simulation is expected to demonstrate the interaction between the space charge distribution and the electric field.

Figure 8 shows the normalized space charge density distribution. Not much can be seen from the distribution map. However, from the line plot given in figure 8(b), one can clearly see the space charge distribution along the x-direction is no longer linear. The space charge distribution is slightly curved up towards the top of the detector. Figure 8(b) also shows the 1-D analytical solution (cf. eq. (A.3). A slight discrepancy between the 3-D numerical solution and the 1-D analytical solution occurs in the middle section of the chamber.

The plots in figure 9 show the field maps of the three components of the electric field at various planes of the detector. Compared to the uniform nominal electric field, the distortion of the electric field is obvious. The distortion is caused by the space charge distribution. E_x is strengthened near the cathode plane and weakened near the anode plane. E_x is symmetric in both the y- and z-directions. E_y and E_z are nonzero. E_y is antisymmetric in the y-direction while E_z is antisymmetric in

2023 JINST 18 P06022

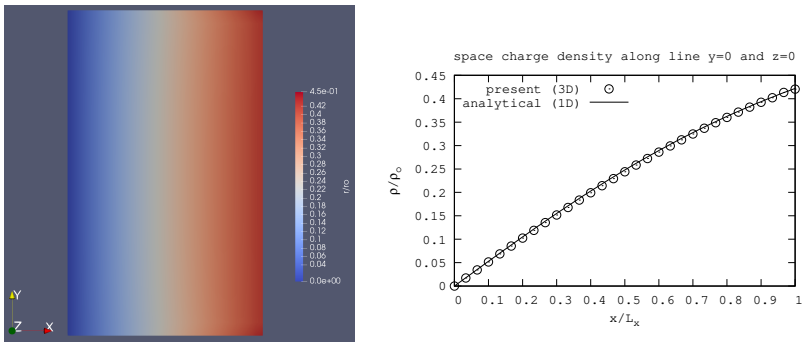

(a) (b)

Figure 8. Case II: space charge density distribution in the $x-y$ plane at $z=0$ (a) and $\rho_c/\rho_\circ$ vs. x/L_x (b).

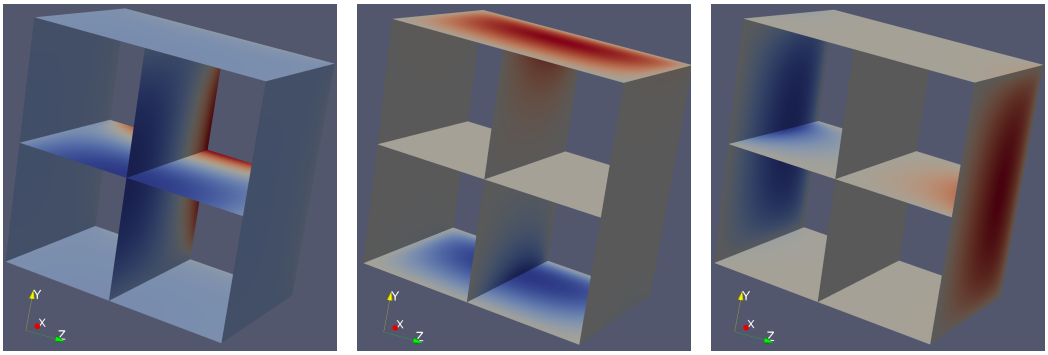

(a) E_x (b) E_y (c) E_z

Figure 9. Case II: electric field maps in the center $x-y$ plane, the center $x-z$ plane and the field cage walls in the case of no background flow field. (a): x-component, (b): y-component and (c): z-component. The anode plane is the near plane perpendicular to the x-axis and the cathode plane is the far plane parallel to the anode plane. Red color and blue color indicate strong and weak electric field, respectively.

the z-direction. The (anti)symmetry is due to the geometric symmetry of the detector in y- and z-directions.

The line plots shown in figure 10 reveal the quantitative information of the distorted electric field components in three representative center lines in the detector. Figure 10(a) shows $E_x/E_\circ$ vs. x/L_x along the center line in the center x-y plane. The 1-D analytical solution derived in ref. [12] (cf. eq. (A.8)) is also shown in figure 10(a). The x-component of the 3-D electric field differs quite noticeably from the 1-D analytical solution especially near the anode and the cathode planes. This is expected, since the electric field is a vector field. The other two line plots in figure 10 show $E_y/E_\circ$ vs. y/L_y and $E_z/E_\circ$ vs. z/L_z whose magnitudes are not negligible. At the anode plane, the weakened E_x is about 94% of the nominal value while at the cathode plane E_x is strengthened to be about 113% of the nominal value. The antisymmetry of the E_y and E_z components are verified in the line plots.

2023 JINST 18 P06022

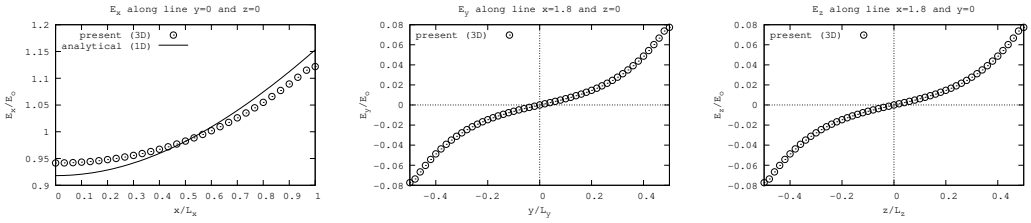

(a) (b) (c)

Figure 10. Case II: electric field line plots. (a): $E_x/E_\circ$ vs. x/L_x along the line defined by $y = 0$ and $z = 0$, (b): $E_y/E_\circ$ vs. y/L_y along the line defined by $x = 1.8$ and $z = 0$, and (c): $E_z/E_\circ$ vs. z/L_z along the line defined by $x = 1.8$ and $y = 0$. The electric field is normalized by the nominal electric field $E_\circ = 500\,\mathrm{V/cm}$.

3.1.3 Case III: the effect of the background flow field

Since the drift velocity of ions is comparable in magnitude to the liquid argon flow field in typical LArTPC detectors, the background flow field is expected to carry the ions around causing the local accumulation of space charges which further distorts the electric field. To simulate this effect, an artificial stationary flow velocity field is constructed. The magnitude of the artificial flow velocity field is intentionally constructed to be twice as large as that of the electric field induced drift velocity. The artificial velocity field is confined in the $x - y$ plane with the following velocity components:

$$u_1 = \frac{1}{180}(x - x_l)^2(x_r - x)^2(y - y_b)(y_t - y)(y_b + y_t - 2y) \tag{3.2a}$$

$$u_2 = -\frac{1}{180}(y - y_b)^2(y_t - y)^2(x - x_l)(x_r - x)(x_l + x_r - 2x) \tag{3.2b}$$

$$u_3 = 0 \tag{3.2c}$$

where $x_l = -3.6$, $x_r = 0.0$, $y_b = -3.0$ and $y_t = 3.0$ which define the $x - y$ dimensions of the detector chamber.

Figure 11 shows the drift velocity field induced by the electric field (a), artificial flow velocity field (b) and the combined velocity field (c). As can be seen, the electric field induced drift velocity field is horizontally directed from the anode plane to the cathode plane. The artificial flow velocity field defined by eqs. (3.2c)–(3.2a) is a counterclockwise vortex circling in the $x - y$ cross section plane of the chamber. From the combined velocity field, it can be noticed that the velocity near the bottom of the detector is strengthened while the velocity near the top of the detector is weakened. The velocity field indicates that the ions will be carried toward the center of the vortex until balance is reached, which is verified by the space charge distribution shown in figure 12.

Figure 13 shows the resulting electric field at various planes and field cage walls of the detector. Comparison between the current electric field with that shown in figure 9 clearly reveals the difference. The distorted electric becomes nonsymmetric in its y- and z-components. E_y and E_z are strengthened near the top of the detector where space charge is accumulated.

2023 JINST 18 P06022

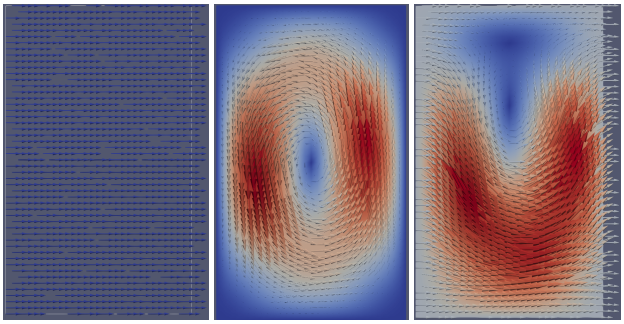

(a) (b) (c)

Figure 11. Case III: velocity field in the center $x - y$ plane at the beginning of the simulation. (a): drift velocity field induced by the electric field, (b): artificial flow field, and (c): combined velocity field.

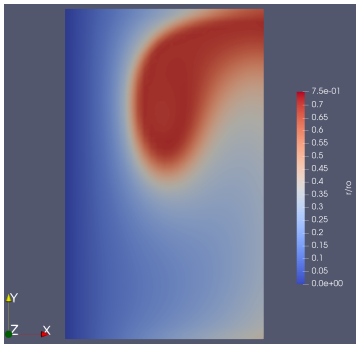

Figure 12. Case III: space charge density distribution in the $x - y$ plane at $z = 0$ in the presence of an artificial background flow velocity field.

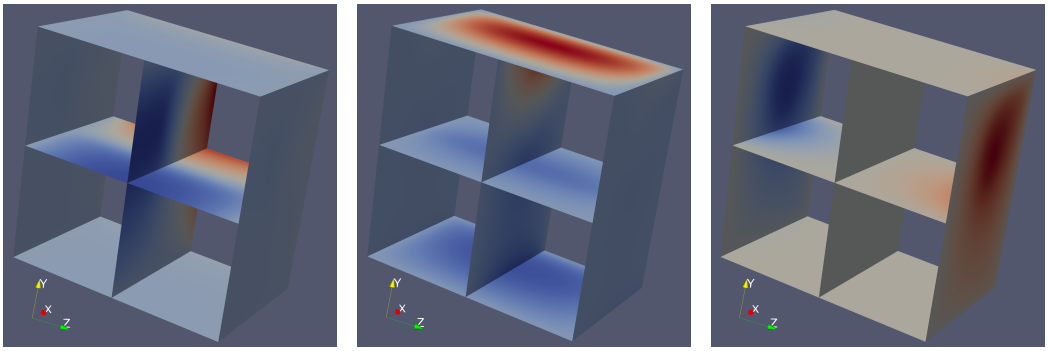

(a) E_x (b) E_y (c) E_z

Figure 13. Case III: electric field in the center $x - y$ plane, the center $x - z$ plane and the field cage walls in the presence of an artificial background flow field. (a): x-component, (b): y-component, and (c): z-component.

2023 JINST 18 P06022

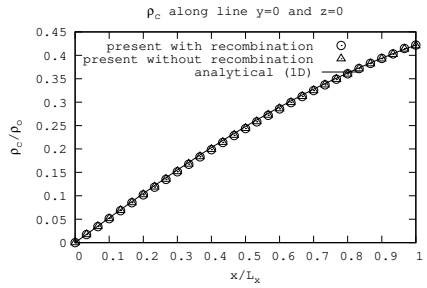

Figure 14. Case II re-run considering the charge recombination.

3.2 Effect of charge recombination

The charge recombination effect can be modeled by multiplying the source term in eq. (1.1) by a recombination function [12, 19] given as follows:

$$R(\mathbf{E}) = 1.15/(1 + 72.9/|\mathbf{E}|) \tag{3.3}$$

which is a function of the electric field. Here $|\mathbf{E}|$ is the magnitude of the electric field in V/cm. We re-run Case II with the above recombination function included. Our numerical result (cf. figure 14) show that the difference in the space charge distribution from that without considering recombination is negligible for the current $\alpha = 0.69758$. The difference in the electric field is also negligible (not shown here) for this small α value. The conclusion is consistent with that given in [12].

3.3 Effect of diffusion

Case III is re-run with the diffusion term included to investigate its effect on the space charge distribution. The diffusion coefficient takes the vale of $D = 1.2134543 \times 10^{-9}\mathrm{m}^2/\mathrm{s}$ according to the Einstein relation (1.3). The computed space charge distribution along the line defined by $y = 1.5$ and $z = 0$ is given in figure 15(a). As indicated in figure 12, the chosen line roughly passes the region where the space charge varies the most. As can be seen in figure 15(a), diffusion has a negligible effect on the space charge distribution.

Figure 15(b) shows the convergence history toward the steady state, which is typical in all simulations presented in this paper.

4 Conclusions and discussions

In this paper, a hybrid finite volume/finite element numerical solver that simulates the interaction between space charge distribution and the electric field in liquid Argon time projection chamber (LArTPC) detectors is described. A cell-centered finite volume method is used to solve the ion transport equation and the finite element method is used to solve the electric potential equation. The interaction between the space charge distribution and the electric field is numerically simulated within each physical time step. The simulation continues until the steady-state has been reached. The comparison with the 1-D analytical solution verifies the accuracy of the current 3-D solver. Several 3-D numerical tests show that the space charge effect on the electric field is noticeable

2023 JINST 18 P06022

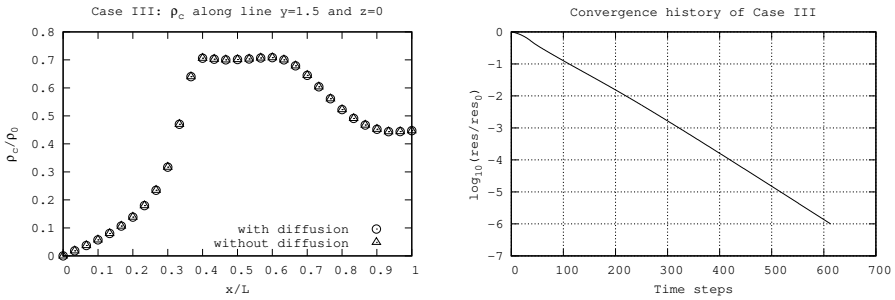

(a) Space charge distribution.

(b) Convergence history.

Figure 15. Case III re-run with diffusion included.

and cannot be neglected in the calculation of the space charge density distribution itself. With the presence of a background flow field, which is comparable in magnitude with the positive ion drift velocity, the distortion of the electric field is more significant. Together with a Computational Fluid Dynamics (CFD) calculation of the background flow velocity, the current solver can serve as a computational tool to investigate the space charge effect on the electric field in particle detectors. A high-accuracy calculation of the space-charge distribution is important in the simulation of the detector performance.

It is worth mentioning the potential impact of uncertainties in the parameters assumed as inputs to the calculation using the current numerical solver. These include the magnitude of the source term, the recombination rate, the Ar^+ ion mobility, the negative ion mobilities (separately for oxygen and water), and the possible variations in the flow field. The flow field calculation, to be described in a future paper, depends on the temperature and flow rate of LAr in the input pipes, the heat leak in the cryostat walls as a function of position, and the porosities of the various detector elements. Data collected by the LArTPC from drifting electrons can be compared with predictions from the space-charge model and the values of uncertain parameters adjusted to maximize the agreement, in a procedure similar to that followed by MicroBooNE [6], but with the detailed model presently described. Residual uncertainties on these parameters after the data-driven fit may be used in models of detectors for which the effect of space charge is difficult to measure, such as the DUNE far detector. Future work will explore the impact of parameter uncertainties on the results.

Furthermore, negatively-charged ions created when electrons attach to impurities (oxygen or water molecules) also are expected to drift slowly, it might be needed to simulate negative ion buildup. In our future work, we will model the O_2^- and H_2O^- ions separately as they have different mobilities and concentrations.

Ongoing work includes simulating the liquid Argon flow using an in-house CFD solver to obtain a realistic flow velocity field. The total electrostatic force on the accumulated space charge in the fluid will be evaluated. The computed realistic flow field will be added to the drift velocity of ions to calculate the distorted electric field using the current space charge solver.

2023 JINST 18 P06022

Acknowledgments

This work is partially supported by U.S. Department of Energy Office of Science Award No. DE-SC0023125, NSF Award No. 2219542 and NASA Award No. 80NSSC21M0332.

This document was prepared using the resources of the Fermi National Accelerator Laboratory (Fermilab), a U.S. Department of Energy, Office of Science, HEP User Facility. Fermilab is managed by Fermi Research Alliance, LLC (FRA), acting under Contract No. DE-AC02-07CH11359.

A Analytical solutions of one-dimensional space charge transport and the electric field

For completeness, the analytical solutions of space charge distribution and electric field in one dimension (1-D) is provided in this appendix. The derivation is adapted from ref. [12]. Attention has been paid to the notational consistency with the current paper.

Ignoring the diffusion term, one has the following steady-state continuity equation for space charge:

$$\nabla \cdot (\rho_c \mathbf{u}_d) = S \tag{A.1}$$

where ρ_c is the space charge density, $\mathbf{u}_d$ is the drift velocity induced by the electric field and S is the source term.

In 1-D, eq. (A.1) becomes

$$\frac{\mathrm{d}(\rho_c u_d)}{\mathrm{d}x} = S$$

which has the following analytical solution

$$\rho_c u_d = Sx + A \tag{A.2}$$

after integration. The integration constant A can be determined as follows. Without loss of generality, assume the anode is located at $x = 0$. Since positive ions drift away from the anode, there should be no accumulation of space charge at the anode at steady state, i.e. $\rho_c = 0$ at $x = 0$. Therefore, the integration constant $A = 0$.

Substituting the drift velocity $u_d = \mu E$ where μ is the mobility and E is the electric field into eq. (A.2) to obtain

$$\rho = \frac{Sx}{\mu E} \tag{A.3}$$

Note that ρ can be normalized by $\rho_\circ$ which is defined as $\rho_\circ \equiv \varepsilon E_\circ / L$ where L is the distance between the anode and the cathode. In addition, ρ is often expressed as a function of x/L. Equation (A.3) can be written as

$$\frac{\rho}{\rho_\circ} = \left(\frac{LS}{\rho_\circ \mu E}\right)\frac{x}{L} \tag{A.4}$$

Gauss's law in 1-D states that

$$\frac{\mathrm{d}E}{\mathrm{d}x} = \frac{\rho}{\varepsilon} \tag{A.5}$$

Combining eqs. (A.3) and (A.5) yields

$$E\mathrm{d}E = \frac{S}{\mu\varepsilon} x \mathrm{d}x$$

2023 JINST 18 P06022

which can be integrated on both sides, namely,

$$\int E\mathrm{d}E = \frac{S}{\mu\varepsilon}\int x\mathrm{d}x$$

The above indefinite integral results in

$$E^2 = \frac{S}{\mu\varepsilon}x^2 + B$$

where B is the integration constant to be determined.

Let the electric field at the anode ($x = 0$) be E_a. Then the integration constant $B = E_a^2$ where E_a remains to be determined. As a result, the electric field, as a function of x, is given by

$$E(x) = \sqrt{\frac{S}{\mu\varepsilon}x^2 + E_a^2} \tag{A.6}$$

Define a dimensionless parameter α as

$$\alpha = \frac{L}{E_\circ}\sqrt{\frac{S}{\mu\varepsilon}} \tag{A.7}$$

where $E_\circ$ is the nominal value of the electric field. Using α, E in eq. (A.6) can be expressed as

$$\frac{E(x)}{E_\circ} = \sqrt{\alpha^2\left(\frac{x}{L}\right)^2 + \left(\frac{E_a}{E_\circ}\right)^2} \tag{A.8}$$

$E(x)$ can be used to determine the electric potential distribution along x. Ref. [12] gives the analytical expression for $V(x)$ as follows

$$V(x) = -\int_0^x E(x')\mathrm{d}x' = -\frac{x}{2}E(x) - \frac{LE_a^2}{2\alpha E_\circ}\ln\left(\frac{E(x)}{E_a} + \frac{\alpha x E_\circ}{LE_a}\right) \tag{A.9}$$

With the boundary condition $V(x = L) = -E_\circ L$, one can determine the values of E_a at the anode by combining eqs. (A.8) and (A.9) to form a nonlinear equation for $E_a/E_\circ$. The nonlinear equation can be solved by the Newton-Raphson iterative method.

References

[1] DUNE collaboration, *Deep Underground Neutrino Experiment (DUNE), Far Detector Technical Design Report, Volume I Introduction to DUNE*, 2020 *JINST* **15** T08008 [arXiv:2002.02967].

[2] DUNE collaboration, *Design, construction and operation of the ProtoDUNE-SP Liquid Argon TPC*, 2022 *JINST* **17** P01005 [arXiv:2108.01902].

[3] DUNE collaboration, *Status of ProtoDUNE Dual Phase*, *PoS* **EPS-HEP2019** (2020) 381 [arXiv:1910.10115].

[4] DUNE collaboration, *Scintillation light detection in the 6-m drift-length ProtoDUNE Dual Phase liquid argon TPC*, *Eur. Phys. J. C* **82** (2022) 618 [arXiv:2203.16134].

2023 JINST 18 P06022

[5] DUNE collaboration, *Deep Underground Neutrino Experiment (DUNE), Far Detector Technical Design Report, Volume IV: Far Detector Single-phase Technology*, 2020 *JINST* **15** T08010 [arXiv:2002.03010].

[6] M. Mooney, *The MicroBooNE Experiment and the Impact of Space Charge Effects*, in the proceedings of the *Meeting of the APS Division of Particles and Fields*, (2015) [arXiv:1511.01563].

[7] DUNE collaboration, *First results on ProtoDUNE-SP liquid argon time projection chamber performance from a beam test at the CERN Neutrino Platform*, 2020 *JINST* **15** P12004 [arXiv:2007.06722].

[8] MicroBooNE collaboration, *Measurement of space charge effects in the MicroBooNE LArTPC using cosmic muons*, 2020 *JINST* **15** P12037 [arXiv:2008.09765].

[9] E.A. Voirin, *LBNF liquid argon CFD simulations*, DUNE Technical Report DUNE-doc-581-v4 (2015).

[10] G.J. Michna, S.P. Gent and A. Propst, *CFD Analysis of Fluid, Heat, and Impurity Flows in DUNE FAR Detector to Address Additional Design Considerations*, DUNE Technical Report DUNE-doc-5915-v1 (2017).

[11] G.J. Michna, S.P. Gent, D. Pederson and C. Streff, *CFD Analysis of the Fluid, Heat, and Impurity Flows in ProtoDUNE Single Phase Detector*, DUNE Technical Report DUNE-doc-17481-v1 (2019).

[12] S. Palestini and F. Resnati, *Space charge in liquid argon time-projection chambers: a review of analytical and numerical models, and mitigation methods*, 2021 *JINST* **16** P01028.

[13] S. Tu and S. Aliabadi, *Development of a hybrid finite volume/element solver for incompressible flows on unstructured meshes*, *Int. J. Numer. Meth. Fluids* **55** (2007) 177.

[14] S. Tu, S. Aliabadi, R. Patel and M. Watts. *An implementation of the Spalart-Allmaras DES model in an implicit unstructured hybrid finite volume/element solver for incompressible turbulent flow*, *Int. J. Numer. Meth. Fluids* **59** (2008) 1051.

[15] Y. Saad, *Iterative methods for sparse linear systems*, PWS Publishing Company (1996).

[16] S. Tu, S. Aliabadi, A. Johnson and M. Watts, *A robust parallel implicit finite volume solver for high-speed compressible flows*, AIAA Paper 2005-1396, January 2005.

[17] G. Karypis, *ParMETIS — parallel graph partitioning and fill-reducing matrix ordering*, https://github.com/KarypisLab/ParMETIS.

[18] A. Johnson and T. Tezduyar, *Parallel computation of incompressible flows with complex geometries*, *Int. J. Numer. Meth. Fluids* **24** (1997) 1321.

[19] S. Amoruso et al., *Study of electron recombination in liquid argon with the ICARUS TPC*, *Nucl. Instrum. Meth. A* **523** (2004) 275.

2023 JINST 18 P06022